Hydrogenation Properties of *Ln*Al$_2$ (*Ln* = La, Eu, Yb), LaGa$_2$, LaSi$_2$ and the Crystal Structure of LaGa$_2$H$_{0.71(2)}$

**Anton Werwein [1], Christopher Benndorf [2], Marko Bertmer [3] , Alexandra Franz [4], Oliver Oeckler [2] and Holger Kohlmann [1,]* **

[1] Leipzig University, Institute of Inorganic Chemistry, Johannisallee 29, 04103 Leipzig, Germany; anton.werwein@uni-leipzig.de
[2] Leipzig University; Institute of Mineralogy, Crystallography and Materials Science, Scharnhorststraße 20, 04275 Leipzig, Germany; christopher.benndorf@uni-leipzig.de (C.B.); oliver.oeckler@uni-leipzig.de (O.O.)
[3] Leipzig University, Felix Bloch Institute for Solid State Physics, Linnéstraße 5, 04103 Leipzig, Germany; bertmer@physik.uni-leipzig.de
[4] Helmholtz-Zentrum Berlin, Hahn-Meitner-Platz 1, 14109 Berlin, Germany; alexandra.franz@helmholtz-berlin.de
[*] Correspondence: holger.kohlmann@uni-leipzig.de; Tel.: +49-341-9736201

Abstract: Many Zintl phases take up hydrogen and form hydrides. Hydrogen atoms occupy interstitial sites formed by alkali or alkaline earth metals and/or bind covalently to the polyanions. The latter is the case for polyanionic hydrides like Sr*Tr*$_2$H$_2$ (*Tr* = Al, Ga) with slightly puckered honeycomb-like polyanions decorated with hydrogen atoms. This study addresses the hydrogenation behavior of *LnTr*$_2$, where the lanthanide metals *Ln* introduce one additional valence electron. Hydrogenation reactions were performed in autoclaves and followed by thermal analysis up to 5.0 MPa hydrogen gas pressure. Products were analyzed by powder X-ray and neutron diffraction, transmission electron microscopy, and NMR spectroscopy. Phases *Ln*Al$_2$ (*Ln* = La, Eu, Yb) decompose into binary hydrides and aluminium-rich intermetallics upon hydrogenation, while LaGa$_2$ forms a ternary hydride LaGa$_2$H$_{0.71(2)}$. Hydrogen atoms are statistically distributed over two kinds of trigonal-bipyramidal La$_3$Ga$_2$ interstitials with 67% and 4% occupancy, respectively. Ga-H distances (2.4992(2) Å) are considerably longer than in polyanionic hydrides and not indicative of covalent bonding. ^{2}H solid-state NMR spectroscopy and theoretical calculations on Density Functional Theory (DFT) level confirm that LaGa$_2$H$_{0.7}$ is a typical interstitial metallic hydride.

Keywords: Zintl phases; metal hydrides; interstitial hydrides; Zintl phase hydrides; lanthanides; powder diffraction; neutron diffraction; deuterides; thermal analysis; solid-state NMR

1. Introduction

Zintl phases are polar intermetallic compounds formed by alkali or alkaline earth metals *M* and a main group element *X* of group 13–16. According to the Zintl–Klemm concept, *M* atoms formally transfer valence electrons to relatively electronegative *X* atoms, which form polyanions with the connectivity of an isoelectronic element [1–6]. K$_4$Si$_4$ is an archetypal example with (Si$_4$)$^{4-}$ tetrahedra akin to P$_4$ tetrahedra in white phosphorous [2]. Zintl phases and related compounds have recently been investigated for potential application, for example as thermoelectric materials (e.g., Mg$_2$Si [7]), in magnetocaloric devices (e.g., Gd$_5$Si$_4$ [8]) or in thin-film solar cells (e.g., BaSi$_2$ [9]).

The hydrogenation of Zintl phases has attracted considerable interest, since the incorporation of hydrogen can influence structures and physical properties (e.g., electrical conductivity, magnetic ordering) in a manifold way [10,11].

Hydrogen gas may oxidize the polyanion, e.g., from X^{x-} to $X^{(x-1)-}$, thus decreasing the valence electron concentration (VEC) and—according to the Zintl–Klemm concept—increasing the connectivity of X atoms [12–14]. Hydrogen atoms are reduced to hydride ions, H^-, during this reaction. They can be incorporated in voids of the crystal structure, e.g., M_4 tetrahedra, or bound covalently to the polyanion. A plethora of structural motifs are observed, e.g., hydrogen-decorated polyanionic sheets ($SrAl_2H_2$ [13]), ribbons ($SrGeH_{4/3-x}$ [14]), chains ($BaSiH_{2-x}$ [15]), or small oligomers ($Ba_3Si_4H_{1-2}$ [16]).

SrGa$_2$ is a classical Zintl phase and crystallizes in the AlB$_2$ structure type with honeycomb-like 6^3 nets of gallium atoms. According to the Zintl–Klemm concept, two electrons of the strontium atom are formally transferred to gallium atoms resulting in the limiting ionic formula $Sr^{2+}(Ga^-)_2$. Ga^- ions are iso-valence-electronic to carbon and form planar graphite-like layers. LaGa$_2$ (AlB$_2$ structure type [17], Figure 1) can be described by the limiting ionic formula $La^{3+}(Ga^-)_2e^-$. In contrast to the electron-precise SrGa$_2$, the compound LaGa$_2$ can be called a metallic or electronically imbalanced Zintl phase, since the excess electrons are mainly located in the conduction band and not transferred to the polyanion [18]. The concept of electronically imbalanced Zintl phases is well known and reported for several other compounds like A_5Pn_3 (A = Ca, Yb, Sm, Eu; Pn = Sb, Bi) [19–21]. A further Zintl phase with an excess electron exhibiting the AlB$_2$ structure-type is SrAlSi ($Sr^{2+}(AlSi)^-e^-$). Both SrGa$_2$ and SrAlSi react with hydrogen to form polyanionic hydrides with covalent Tr-H (Tr = Al, Ga) bonds. SrGa$_2$D$_2$ is isostructural to SrAl$_2$D$_2$, where all atoms of the polyanion connect to one hydrogen atom, while in SrAlSiD only aluminium atoms bind to hydrogen [22,23]. Hydrogenation thus transforms the electronically imbalanced (metallic) Zintl phase SrAlSi to an electron-precise Zintl phase hydride SrAlSiH. Metallic Zintl phases $LnTt$ (Ln = La, Nd; Tt = Si, Ge, Sn) react in the same manner and take up hydrogen to form electron-precise Zintl phase hydrides $LnTt$H [24]. The metallic Zintl phase LaSi$_2$ adopts the ThSi$_2$ structure type, which is characterized by a trigonal prismatic surrounding of silicon atoms by lanthanum atoms and a three-dimensional silicon network (Figure 1) [25]. The reactivity of LaSi$_2$ towards hydrogen was found to be very low [26].

So far, only interstitial hydrides were observed for Zintl phases containing lanthanide elements. The quest for polyanionic hydrides of lanthanide Zintl phases is still open. In this work, we (re)investigate the hydrogenation behavior of the metallic Zintl phases LaGa$_2$ and LaSi$_2$ and of the cubic Laves phases $LnAl_2$ (Ln = La, Eu, Yb, MgCu$_2$ type [27], Figure 1) in order to further elucidate crystal structure and bonding in their hydrides.

Thermal analysis under hydrogen atmosphere was used to characterize the reactivity towards hydrogen. Since hydrogenation reactions often do not yield single crystals, structural investigation was based on powder diffraction. Due to the low scattering power of hydrogen for X-rays, neutron diffraction was carried out for the structural analysis of a deuterated sample of LaGa$_2$. ^{2}H as a quadrupolar nucleus was also used for probing the local structure by NMR spectroscopy and DFT calculations gave insight into the electronic changes upon hydrogenation.
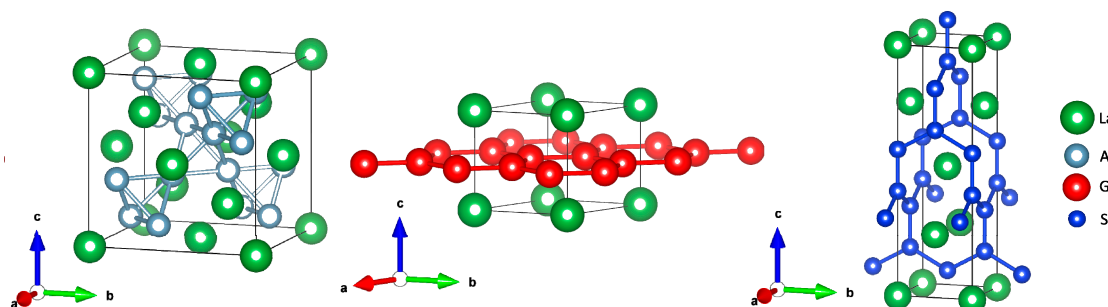

Figure 1. Crystal structures of LaAl$_2$ (MgCu$_2$ type, **left**), LaGa$_2$ (AlB$_2$ type, **middle**), and LaSi$_2$ (ThSi$_2$ type, **right**). The polyanionic networks are emphasized.

2. Materials and Methods

Synthesis: Due to air sensitivity, all handlings were carried out in an argon-filled glove box. Intermetallic compounds with lanthanum were synthesized from the elements in stoichiometric amounts (La: smart-elements (Vienna, Austria), ≥99.99%, surface cleaned mechanically, cut into small pieces; Si: abcr (Karlsruhe, Germany), 99.9999%; Al, Ga: Smart elements, 99.99%) by fusing the starting materials in a water-cooled copper crucible of an arc furnace under 80 kPa argon atmosphere (dried over P_4O_{10}, molecular sieve, silica gel and titanium sponge at 800 K). Ingots were turned over and remelted several times to ensure homogeneity. $EuAl_2$ and $YbAl_2$ were prepared from stoichiometric mixtures of the elements (Eu: Chempur (Karlsruhe, Germany), 99.9%; Yb: Kristallhandel Kelpin (Leimen, Germany), 99.9%) in sealed tantalum ampules, which were heated under dynamic vacuum in a silica-glass tube at 1423 K for 4 h and cooled by switching off the furnace. The hydrides (deuterides) were prepared from well-ground samples of the intermetallic precursors in crucibles made from hydrogen-resistant Böhler (Kapfenberg, Austria) L718-V alloy and reacted with hydrogen (deuterium) gas (hydrogen: Air Liquide (Paris, France), 99.9%; deuterium, Air Liquide (Paris, France), 99.8%) at 2.0 MPa in autoclaves made from the same alloy. The temperature was increased with a rate of 100 K/h to 573 K, held for 48 h, and cooled by switching off the furnace.

Elemental Analysis: The hydrogen contents of the hydrides were determined by elemental analysis with a VARIO EL (Elementar Analysensysteme GmbH, Hanau, Germany) microanalyzer using the carrier gas-hot extraction method in triplicate repetition.

Thermal Analysis: Hydrogenation experiments were carried out in a differential scanning calorimeter (DSC) Q1000 from TA Instruments (New Castle, Delaware, USA) equipped with a gas pressure cell. Powdered samples weighing 10–30 mg were loaded into aluminum pans, which were subsequently crimped. The experiments were performed under isochoric conditions with a heating rate of 10 K/min under 5.0 MPa hydrogen at 298 K, which increased to 6.7 MPa at the final temperature of 703 K.

Powder X-Ray Diffraction (PXRD) Powder X-ray diffraction data were collected on a Huber (Rimsting, Germany) G670 camera with image-plate detection system using Mo-Kα_1 or Cu-Kα_1 radiation. Flat transmission samples were prepared by grinding and mixing the moisture sensitive powders with Apiezon grease under an argon atmosphere and placing the sample between two sheets of Kapton foil.

Powder Neutron Diffraction (PND): Powder neutron diffraction was carried out at the E9 diffractometer (λ = 1.7982(1) Å) at Helmholtz-Zentrum Berlin für Materialien und Energie, Berlin, Germany [28]. Powdered samples (3 g) were held in gas-tight vanadium containers with 6 mm inner diameter and the measurement time was 8 h. Deuterides instead of hydrides were used in order to avoid the high incoherent scattering of [1]H.

Rietveld Refinement: Rietveld refinements [29,30] were performed using TOPAS [31] and FULLPROF [32,33]. Deuterium atoms were located by difference Fourier analysis. Crystal structures were visualized with VESTA [34,35]. Further details of the crystal structure investigations may be obtained from FIZ Karlsruhe, 76344 Eggenstein-Leopoldshafen, Germany (fax: (+49)7247-808-666; e-mail: crysdata@fiz-karlsruhe.de, on quoting the deposition number CSD-1885556 ($LaGa_2D_{0.71(2)}$).

Density Functional Theory (DFT) Calculation: DFT calculations were performed with the Abinit software package [36–40] using generalized gradient approximation (GGA) and the Perdew–Burke–Ernzerhof (PBE) functional [41]. Projector augmented wave (PAW) [42] atomic data were taken from the JTH PAW atomic dataset table [43,44]. The convergence of calculations was tested regarding kinetical energy cutoff, k-point grid and smearing of metallic occupation levels with an accuracy of 0.1 mHartree. The kinetical energy cutoff (ecut) was set to 35 Hartree (pawecutdg = 70 Hartree). The compounds were treated metallic with 1 mHartree Gaussian smearing (occopt = 7, tsmear = 0.001). The smearing contribution of the total energy was lower than 0.1 mHartree. The hydrogen-containing structures were treated similarly. For structure relaxation a 5 × 5 × 4 ($LaGa_2$) and 5 × 5 × 2 ($LaGa_2H$) Monkhorst-Pack-grid was applied [45]. Lattice parameters reproduce experimental data with less than

1% deviation. The density of states was calculated using a $10 \times 10 \times 8$ ($LaGa_2$) and $10 \times 10 \times 4$ ($LaGa_2H$) k-grid and integration was performed using the tetrahedron method.

Transmission Electron Microscopy (TEM): A deuterated sample $LaGa_2D_x$ was investigated using a Philips (Amsterdam, Netherland) CM-200 STEM transmission electron microscope (acceleration voltage 200 kV, super twin objective lens, point resolution 0.23 nm) equipped with an EDAX (Mahwah, NJ, USA) energy-dispersive X-ray spectroscopy (EDX) system. A small amount of the sample (approx. 10 mg) was crushed under cyclohexane to a fine powder using an agate mortar. The suspension was allowed to sediment for a few seconds and subsequently one drop of the supernatant suspension was cast on a copper grid coated with holey carbon film (mesh 200; Plano, Wetzlar, Germany). The investigation was carried out using a double-tilt low-background sample holder (Gatan, Pleasanton, CA, USA). EDX analysis was conducted at several areas of the examined crystal (Figure S7 in Supplementary Materials). Kinematical selected-area electron diffraction (SAED) patterns (Figures S8–S10 in Supplementary Materials) were simulated using the JEMS software package [46,47].

Solid-state NMR: ^2H NMR measurements were performed with a Bruker Avance spectrometer (Bruker Corporation, Billerica, MA, USA) equipped with a $B_0 = 17.6$ T superconducting magnet (frequency 114.92 MHz for ^2H). For both static and MAS experiments (5 kHz spinning frequency) a 2.5 mm MAS probe was used. A one-pulse sequence with a 90° pulse length of 7 μs and a recycle delay of 10 s was used. About 1000 scans were recorded.

3. Results

3.1. Hydrogenation Reactions

The hydrogenation of $LaGa_2$ at 2.0 MPa deuterium pressure and 573 K yields a new phase with a very similar X-ray powder diffraction pattern. A Rietveld refinement based on the structure model of $LaGa_2$ shows a decrease of the *c* lattice parameter from 4.42521(7) Å to 4.33290(5) Å while the *a* lattice parameter slightly increases from 4.30975(5) Å to 4.32682(3) Å. This results in a negative volume change, which is known for lanthanide-containing hydrides undergoing a metal-semiconductor transition, e.g., $LaH_2 + \frac{1}{2} H_2 \rightarrow LaH_3$ [48,49]. The hydrogen content according to elemental analysis is 0.58(1) hydrogen atoms per formula unit, corresponding to a composition $LaGa_2H_{0.58}$.

The cubic Laves phases $LnAl_2$ (Ln = La, Eu, Yb) decompose during the hydrogenation reaction at 5.0 MPa hydrogen pressure and 773 K to binary hydrides LnH_2 and aluminium-rich phases (La_3Al_{11}, $EuAl_4$, $YbAl_3$; Figures S1–S5 in Supplementary Materials). Differential scanning calorimetry (DSC) of $EuAl_2$ at 5.0 MPa shows a strong exothermic signal at 700 K in accordance with the above-mentioned reaction, while the hydrogenation of $YbAl_2$ does not yield any thermal signal under the same conditions. Additionally, the hydrogenated sample still contains $YbAl_2$ as a minor phase, suggesting a slow reaction.

The powder X-ray diffraction pattern of $LaSi_2$ remains unchanged upon treatment at 773 K and 5.0 MPa hydrogen in an autoclave for 48 h (Figure S6 in Supplementary Materials). The lattice parameters before (*a* = 4.31565(3) Å, *c* = 13.8483(1) Å) and after (*a* = 4.31565(3) Å, *c* = 13.8407(1) Å) hydrogenation do not differ significantly, indicating little, if any reaction with hydrogen.

3.2. Crystal Structure of $LaGa_2D_{0.71(2)}$

In order to locate hydrogen in the crystal structure of hydrogenated $LaGa_2$, neutron powder diffraction was carried out on a deuterated sample. The powder neutron diffraction pattern shows superstructure reflections, which were not observed in X-ray diffraction patterns (Figure 2), indicating a symmetry reduction with respect to hydrogen-free $LaGa_2$ caused by deuterium atoms. A crystal structure model with a doubled *c* lattice parameter accounts for all reflections and was used for Rietveld refinements. Deuterium atoms were located in trigonal-bipyramidal La_3Ga_2 voids by difference Fourier analyses. Rietveld refinements based on this structure model (Table 1) and accounting for small amounts of the secondary phase $LaGaD_x$ show good agreement between measured and calculated powder neutron diffraction patterns (Figure 2). The formation of the superstructure can be explained

by an ordering of deuterium atoms with alternating occupancies of 67(1)% and 4.5(8)% along [001] (Figure 3, Table 1). The gallium layers are closer to the deuterium position with lower occupancy (Figure 3). This results in two different Ga-D distances (2.099(3) Å and 2.247(3) Å). The crystal structure of $LaGa_2D_{0.71(2)}$ is the first example of a Zintl phase hydride derived from the AlB_2 type with a lanthanide. $CeGa_2D_{0.6}$ might be another example, but deuterium positions are not known yet [50]. $LaGa_2D_{0.71}$ and $CeGa_2D_{0.6}$ exhibit similar hydrogen contents and lattice parameter changes during hydrogenation. In contrast to the polyanionic hydrides $SrAl_2H_2$ and $SrAlSiH$ with stoichiometric composition, $LaGa_2H_{0.71(2)}$ is better described as an interstitial hydride with a variable composition. This is supported by the variable unit cell volumes for different samples of $LaGa_2H_x$ ($V = 70.424(3)$ Å^3 to $70.688(3)$ Å^3).
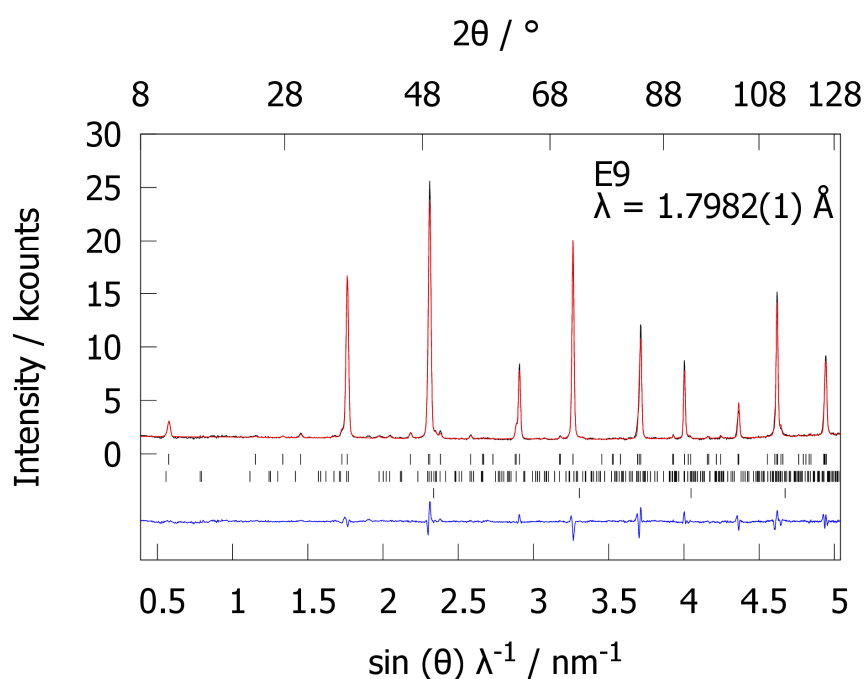

Figure 2. Rietveld refinement of the crystal structure of $LaGa_2D_{0.71(2)}$ based on powder neutron diffraction data (black, E9 at Helmholtz-Zentrum Berlin; red: calculated pattern), $R_p = 3.96\%$, $R_{wp} = 5.55\%$, Bragg makers from top to bottom: $LaGa_2D_{0.71(2)}$ (97.2(8)%), $LaGaD_x$ (2.8(2)%), V (sample container); the difference plot is depicted in blue.
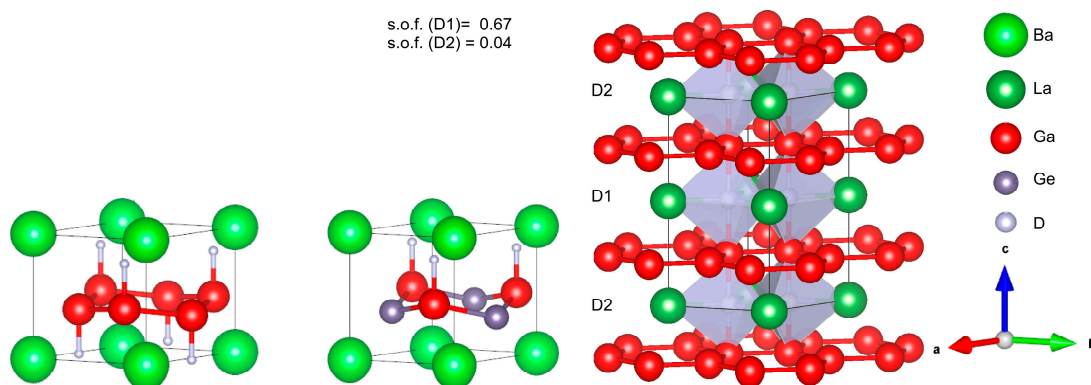

Figure 3. Crystal structures of $BaGa_2D_2$ (**left**), $BaGaGeD$ (**middle**) and $LaGa_2D_{0.71(2)}$ (**right**). Covalent bonds of the polyanions are emphasized.

The good agreement between experimental and calculated SAED patterns of $LaGa_2D_{0.71(2)}$ confirms the structure model derived by neutron diffraction (Figures S8–S10 in Supplementary

Materials). Comparison of the simulated SAED patterns for both structure models and equivalent directions ([112] for LaGa$_2$ and [111] for LaGa$_2$D$_x$, respectively) of experimental data clearly indicates the presence of a two-fold superstructure (Figure S10 in Supplementary Materials). TEM-EDX analysis of the investigated crystal yields an atomic ratio of 33.5(6)% La and 66.5(6)% Ga (averaged over seven individual point measurements) are in good agreement with the crystal structure model (Table 1).

Table 1. Structural parameters of LaGa$_2$D$_{0.71(2)}$, space group *P*6/*mmm*, *a* = 4.3287(3) Å, *c* = 8.6910(5) Å.

Atom	Site	*x*	*y*	*z*	B_{iso}/Å^2	*s.o.f.*
La1	1*a*	0	0	0	0.64(6)	1
La2	1*b*	0	0	1/2	B_{iso}(La1)	1
Ga	4*h*	2/3	1/3	0.2415(3)	0.78(6)	1
D1	2*c*	2/3	1/3	1/2	3.4(2)	0.672(10)
D2	2*d*	2/3	1/3	0	B_{iso}(D1)	0.045(8)

The comparison of LaGa$_2$H$_{0.71(2)}$ with other Zintl phase hydrides derived from the AlB$_2$ structure type reveals interesting structural differences. Both electron-precise *Ae*Ga$_2$ and electronically imbalanced *Ae*GaGe (*Ae* = Sr, Ba) take up hydrogen to form the polyanionic hydrides *Ae*Ga$_2$H$_2$ and *Ae*GaGeH [12]. In these hydrides, bond lengths within the polyanion (Ga-Ga, Ga-Ge, Ge-Ge) are 1.7%–3.2% longer than in the hydrogen-free Zintl phases, as compared to only 0.4% for LaGa$_2$H$_{0.71}$ (all data for deuterides, Table 2). The chemical bonding within the polyanions can change tremendously upon hydrogenation: either π* states are depopulated and the Ga-Ga bonds contract or π states are depopulated and the bond expands [24]. The effect of the hydrogenation on the *E-E* bond length is comparably small for LaGa$_2$H$_{0.71(2)}$ with respect to other Zintl phase hydrides (Table 2). The expansion of the Ga-Ga bond lengths in SrGa$_2$D$_2$ and BaGa$_2$D$_2$ can be explained by the depopulation of π states. In contrast, the oxidation of LaGa$_2$ only depopulates La *d* states (*vide infra*, Section 3.4) and, hence, has little influence on Ga-Ga distances.

The most significant structural difference between the hydrides is the coordination of hydrogen atoms. While hydrogen atoms in SrGa$_2$H$_2$, BaGa$_2$H$_2$ and BaGaGeH are tetrahedrally coordinated by metal atoms with one covalent Ga-H bond, hydrogen atoms in LaGa$_2$H$_{0.71}$ are located in trigonal bipyramidal La$_3$Ga$_2$ voids. This kind of fivefold coordination for hydrogen was also observed in ZrBe$_2$H$_{1.49}$ [51].

The Ga-D distances in SrGa$_2$D$_2$, BaGa$_2$D$_2$, SrGeGaD and BaGeGaD are in the typical range of covalent Ga-D bonds while those in LaGa$_2$D$_{0.71}$ are much longer (Table 2). The Sr-D and Ba-D bond lengths (Table 2) are comparable with bond lengths in mainly ionic compounds such as SrD$_2$ and BaD$_2$ [52,53]. The distances La-D (Table 2), however, are comparable to those in typical interstitial metallic hydrides, e.g., LaNi$_3$D$_{2.8}$ [54].

The *c/a* ratio is an important indicator for the anisotropy of chemical bonding in layered structures, which may be changed considerably upon hydrogenation. For the discussed examples it proves difficult to find a clear tendency. While *c/a* decreases upon hydrogenation for the compounds BaGa$_2$ and LaGa$_2$, it stays nearly the same for SrGa$_2$ and even increases in the case of BaGeGa and SrGeGa (Table 2). It seems that, in addition to the VEC, the size of the cation plays an important role for the spatial demand of the layers.

Table 2. Interatomic distances, their relative changes upon deuteration and lattice parameter ratios of Zintl phases *M*Ga$_2$ (*M* = Sr, Ba, La), *Ae*GaGe (*Ae* = Sr, Ba) and their deuterides.

Zintl Phase	*d*(X-X)/Å	*c/a*	Deuteride	*d*(X-X)/Å	Δ*d*/*d*	*d*(M-D)/Å	*d*(Ga-D)/Å	*c/a*
SrGa$_2$ [55]	2.5122(11)	1.07	SrGa$_2$D$_2$ [56]	2.5569(10)	1.8%	2.5855(9)	1.686(6)	1.07
BaGa$_2$ [55]	2.5511(11)	1.14	BaGa$_2$D$_2$ [56]	2.6333(6)	3.2%	2.6834(6)	1.689(3)	1.08
SrGaGe [57]	2.46632(6)	1.10	SrGaGeD [58]	2.5075(4)	1.7%	2.4824(3)	1.7248(15)	1.17
BaGaGe [57]	2.50287(6)	1.17	BaGaGeD [58]	2.5552(4)	2.1%	2.5878(4)	1.7115(8)	1.20
LaGa$_2$	2.48824(10)	1.02	LaGa$_2$D$_{0.71(2)}$	2.49918(18)	0.4%	2.49918(18)	2.099(3)	1
							2.247(3)	

3.3. Solid-State NMR

^{2}H solid-state NMR spectroscopy was performed as a local probe for metal-deuterium interactions in LaGa$_2$D$_{0.71(2)}$ (see Figure 4). As the ^{2}H nucleus exhibits a spin quantum number of $I = 1$, the quadrupolar coupling can give evidence about covalent bonding. As shown for Zintl phase hydrides of silicon, germanium and tin, covalently bonded deuterium atoms show a distinct quadrupolar coupling due to the presence of strong electric field gradients (EFG), whereas investigations of deuterides with D atoms located in tetrahedral voids formed by alkaline earth atoms yield isotropic line spectra [14]. The static and 5 kHz ^{2}H MAS spectra (Figure 4) of LaGa$_2$D$_{0.71(2)}$ show no indication of covalent interactions that should be visible by a quadrupolar powder pattern (Pake doublet) in the static spectrum. The static linewidth is in the order of 6.5 kHz and can to a large extent be explained by dipolar coupling of deuterium nuclei with other NMR-active nuclei in the vicinity, i.e. ^{2}H, ^{69}Ga/^{71}Ga, and ^{139}La atoms. Calculating the total second moment [59] from all NMR-active spins yields a linewidth of 4.5 kHz. The difference to the experimentally observed one results from the residual linewidth present under MAS (2.2 kHz). The reason for this broad line is not fully understood. It could arise from chemical shift variations due to slight differences in the local atomic environment of deuterium atoms. However, the NMR results suggest that deuterium is not covalently bound, in agreement with the results of the crystal structure determination and crystal chemical considerations (Section 3.2).
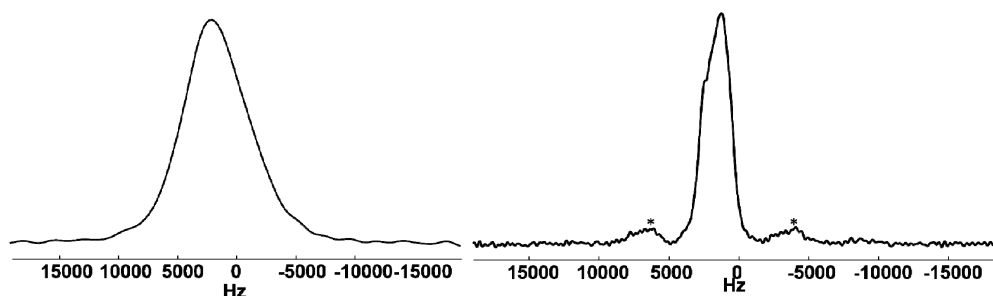

Figure 4. Static (**left**) and MAS (**right**) solid-state ^{2}H NMR spectra of LaGa$_2$D$_{0.71(2)}$, asterisks indicating spinning sidebands.

3.4. Density Funtional Theory (DFT) Calcalations

Three models were used for quantum-mechanical modelling on DFT level, the hydrogen free Zintl phase, a hydride with one (LaGa$_2$H) and a hydride with two hydrogen atoms per formula unit (LaGa$_2$H$_2$) (Tables S1–S3 in Supplementary Materials). The latter is a hypothetical model for evaluating the chances for higher hydrogen contents, e.g., at higher hydrogen pressures. For the calculation of LaGa$_2$ and LaGa$_2$H$_2$, a simple AlB$_2$ type model was used, while the calculation for LaGa$_2$H was performed with only one of the two experimentally found H-atom positions (Table 1). The lattice parameters of LaGa$_2$ calculated by structure optimization are in good agreement with experimental values (Figure S11 and Tables S1–S3 in Supplementary Materials). For LaGa$_2$H ($a = 4.351$ Å, $c = 4.320$ Å), the lattice parameter c is decreased and for LaGa$_2$H$_2$ ($a = 4.289$ Å, $c = 4.570$ Å) it is expanded with respect to the parent compound LaGa$_2$ ($a = 4.3474$ Å, $c = 4.4085$ Å). This observation is in agreement with the experimentally obtained structure model for LaGa$_2$D$_{0.71(2)}$. The slight deviation of the lattice parameter c is attributed to the lower hydrogen content in the experimental structure (LaGa$_2$H$_{0.71}$ vs. LaGa$_2$H). The Ga-H distance of 2.238 Å in the DFT-optimized LaGa$_2$H matches the experimental value well.

The density of states at the Fermi level has a large d contribution from lanthanum for the Zintl phase, emphasizing the metallic character of LaGa$_2$ (Figure 4), while electrons at the Fermi level in *AeTr*$_2$ and *AeTrTt* (*Ae* = Ca, Sr, Ba; *Tr* =Al, Ga; *Tt* = Si, Ge) are rather located in the polyanion [56,58,60]. This is supported by the expansion of the bond lengths in the polyanion for alkaline-earth-containing compounds, while the Ga-Ga distance in LaGa$_2$H$_{0.71}$ is almost unaffected, since mostly d states are depopulated.

This finding supports the limiting ionic formula $La^{3+}(Ga^-)_2e^-$ where the excess electron is in the conduction band. The density of states of $LaGa_2H$ shows a pseudo-gap at the Fermi level, which is quite common for hydrogenated Zintl phases [14,15,24]. The limitations of DFT methods in predicting bandgaps should be kept in mind, however. In comparison, the hydrides $AeTr_2H_2$ show pseudo-bandgaps as well, suggesting poor metallic conductivity [56], but $AeTrTtH$ (Ae = Ca, Sr, Ba; Tr = Al, Ga; Tt = Si, Ge) are small band semiconductors [58,60]. Even though the structures of the different hydrides and the electron counts are similar, the consequences for the electronic properties are tremendous.

The contribution of gallium states at the Fermi level is very small (Figure 4). This finding explains the small expansion of the Ga-Ga bonds during hydrogenation, while the Ga-p contribution of $SrGa_2$ is noticeably higher [55] and leads to a stronger expansion of Ga-Ga bonds.

The partial DOS for hydrogen atoms shows a large dispersion of the *s* band from −7 eV to 0 eV (Figure 5), which can be an indicator for a strong interaction of hydrogen atoms with all surrounding atoms as typical for metallic hydrides.
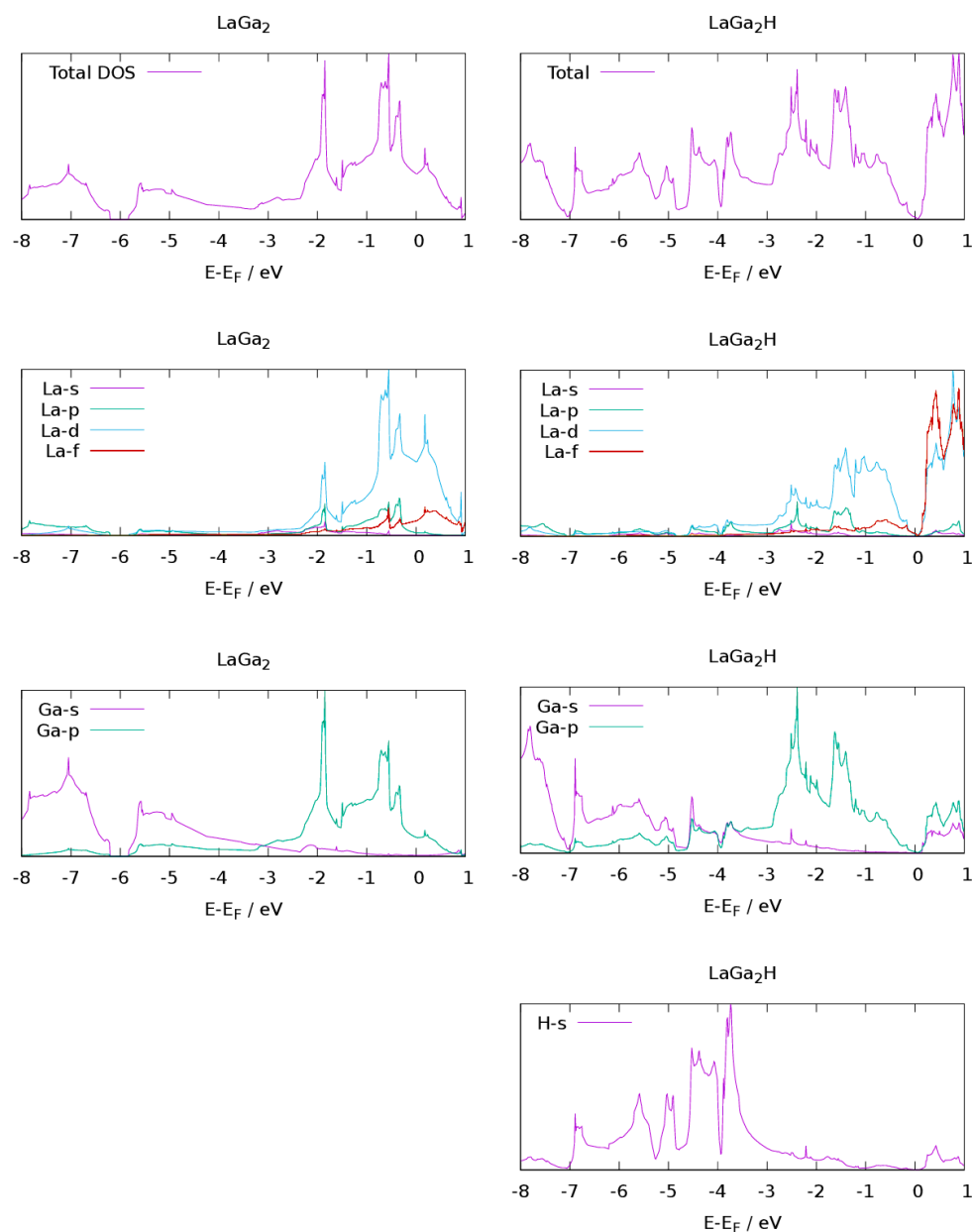

Figure 5. Total (tDOS) and l-resolved partial (pDOS) density of states of $LaGa_2$ and $LaGa_2H$; energies are referenced to the Fermi level.

4. Discussion

The Laves phases $LaAl_2$, $EuAl_2$, and $YbAl_2$ decompose into binary hydrides and aluminum-rich phases upon reaction with hydrogen. Despite the crystal-chemical similarity between europium and strontium, no analogous hydrides were formed. $LaSi_2$ does not react with hydrogen up to 773 K and 5.0 MPa hydrogen even though it features trigonal-bipyramidal La_3Si_2 voids (in analogy to La_3Ga_2 in $LaGa_2$).

The electronically imbalanced Zintl phase $LaGa_2$ forms a metallic hydride with a nearly unchanged heavy atom structure. During the hydrogenation, *d*-states of lanthanum atoms are depopulated. Hydrogen atoms are incorporated in trigonal-bipyramidal La_3Ga_2 voids. The hydrides *AeTr*$_2$*H*$_2$, *AeTrTt*H and $LaGa_2H_{0.71}$ show pronounced differences with respect to the bonding character and electronic properties. Even though the VECs of $LaGa_2$ and *AeTrTt* are equal, the incorporation of hydrogen atoms differs strongly. Compounds *AeTrTt*H exhibit covalent *Tr*-H bonds, comparable to those in *AeTr*$_2$*H*$_2$, while $LaGa_2H_{0.71}$ is a metallic hydride with hydrogen atoms in interstitial voids. The changes of the *Tr-Tr* and *Tr-Tt* bond lengths during hydrogenation suggest that the incorporation of hydrogen depopulates the π states of *AeTr*$_2$ and *AeTrTt*, while the hydrogenation of $LaGa_2$ mainly affects the *d*-states of lanthanum. The DOS of the pristine Zintl phases and their corresponding hydrides confirms this suggestion. The electronic properties of the corresponding hydrides are even more remarkable. While *AeTrTt*H and $LaGa_2H$ are narrow-bandgap semiconductors, *AeTr*$_2$*H*$_2$ remains metallic according to DFT calculations, although covalent *Tr*-H bonds are formed.

So far, covalent *Tr*-H or *Tt*-H (*Tr* = Al, Ga, In; *Tt* = Si, Ge, Sn) bonds in Zintl phase hydrides with lanthanide elements *Ln* are elusive. The strong *Ln*-H interaction seems to dominate chemical bonding, while covalent *Tr*-H or *Tt*-H bonds are competitive only with respect to the somewhat weaker *Ae*-H bonds. This leads to the occupation of interstitials with trigonal-bipyramidal (La_3Ga_2) or tetrahedral (Ln_4) voids by hydrogen atoms for the lanthanide containing compounds and the exclusive formation of covalent *Tr*-H or *Tt*-H bonds for alkaline earth or alkali metal containing compounds. These examples emphasize the subtle influence of properties of Zintl phases and their hydrides due to small changes in element and/or electron count and show a potential way to tune electronic properties by an elegant combination of elements. Zintl phases with alkaline earth, lanthanide and *Tr* or *Tt* elements are an obvious target for further exploration of bonding situations in this class of compounds.

Supplementary Materials: Further data on thermal analyses, X-ray diffraction, selected-area electron diffraction and DFT calculations are available online at http://www.mdpi.com/2073-4352/9/4/193/s1.

Conflicts of Interest: The authors declare no conflict of interest.

References

1. Zintl, E.; Kaiser, H. Über die Fähigkeit der Elemente zur Bildung negativer Ionen. *Z. Anorg. Allg. Chem.* **1933**, *211*, 113–131. [CrossRef]
2. Schäfer, H.; Eisenmann, B.; Müller, W. Zintl-Phasen: Übergangsformen zwischen Metall- und Ionenbindung. *Angew. Chem.* **1973**, *85*, 742–760. [CrossRef]
3. Nesper, R. Chemische Bindungen—Intermetallische Verbindungen. *Angew. Chem.* **1991**, *103*, 805–834. [CrossRef]
4. Kauzlarich, S.M. *Chemistry, Structure and Bonding of Zintl Phases and Ions*; Wiley-VCH: Weinheim, Germany, 1996; ISBN 978-0-471-18619-9.
5. Nesper, R. The Zintl-Klemm Concept—A Historical Survey. *Z. Anorg. Allg. Chem.* **2014**, *640*, 2639–2648. [CrossRef]

6. Corbett, J.D. Polyanionic Clusters and Networks of the Early p-Element Metals in the Solid State: Beyond the Zintl Boundary. *Angew. Chem. Int. Ed.* **2000**, *39*, 670–690. [CrossRef]

7. Akasaka, M.; Iida, T.; Matsumoto, A.; Yamanaka, K.; Takanashi, Y.; Imai, T.; Hamada, N. The thermoelectric properties of bulk crystalline *n*- and *p*-type Mg_2Si prepared by the vertical Bridgman method. *J. Appl. Phys.* **2008**, *104*, 013703. [CrossRef]

8. Gschneidner, K.A., Jr.; Pecharsky, V.K. Magnetocaloric Materials. *Annu. Rev. Mater. Sci.* **2000**, *30*, 387–429. [CrossRef]

9. Toh, K.; Saito, T.; Suemasu, T. Optical Absorption Properties of $BaSi_2$ Epitaxial Films Grown on a Transparent Silicon-on-Insulator Substrate Using Molecular Beam Epitaxy. *Jpn. J. Appl. Phys.* **2011**, *50*, 068001. [CrossRef]

10. Simon, A. Oxidation durch Wasserstoff in der Chemie und Physik der Seltenerdmetalle. *Angew. Chem.* **2012**, *124*, 4354–4361. [CrossRef]

11. Ångstrom, J.; Johansson, R.; Sarkar, T.; Sørby, M.H.; Zlotea, C.; Andersson, M.S.; Nordblad, P.; Scheicher, R.H.; Häussermann, U.; Sahlberg, M. Hydrogenation-Induced Structure and Property Changes in the Rare- Earth Metal Gallide NdGa: Evolution of a $[GaH]^{2-}$ Polyanion Containing Peierls-like Ga−H Chains. *Inorg. Chem.* **2016**, *55*, 345–352. [CrossRef] [PubMed]

12. Häußermann, U. Coexistence of hydrogen and polyanions in multinary main group element hydrides. *Z. Kristallogr.* **2008**, *223*, 628–635. [CrossRef]

13. Häussermann, U.; Kranak, V.F.; Puhakainen, K. Hydrogenous Zintl Phases: Interstitial Versus Polyanionic Hydrides. In *Zintl Phases. Structure and Bonding*; Fässler, T., Ed.; Springer: Berlin/Heidelberg, Germany, 2010; Volume 139, ISBN 978-3-642-21150-8.

14. Auer, H.; Guehne, R.; Bertmer, M.; Weber, S.; Wenderoth, P.; Hansen, T.C.; Haase, J.; Kohlmann, H. Hydrides of Alkaline Earth−Tetrel (AeTt) Zintl Phases: Covalent Tt−H Bonds from Silicon to Tin. *Inorg. Chem.* **2017**, *56*, 1061–1071. [CrossRef]

15. Auer, H.; Schlegel, R.; Oeckler, O.; Kohlmann, H. Structural and Electronic Flexibility in Hydrides of Zintl Phases with Tetrel-Hydrogen and Tetrel-Tetrel Bonds. *Angew. Chem. Int. Ed.* **2017**, *56*, 12344–12347. [CrossRef] [PubMed]

16. Kranak, V.F.; Benson, D.E.; Wollmann, L.; Mesgar, M.; Shafeie, S.; Grins, J.; Häussermann, U. Hydrogenous Zintl Phase Ba_3Si_4Hx (x = 1–2): Transforming Si_4 "Butterfly" Anions into Tetrahedral Moieties. *Inorg. Chem.* **2014**, *53*, 756–764. [CrossRef] [PubMed]

17. Laves, F. Die Kristallstrukturen von $CaGa_2$, $LaGa_2$ und $CeGa_2$. *Naturwissenschaften* **1943**, *11–13*, 145. [CrossRef]

18. Harima, H.; Yanase, Y. Electronic Structure and Fermi Surface of $LaGa_2$. *J. Phys. Soc. Jpn.* **1991**, *60*, 2718–2723. [CrossRef]

19. Leon-Escamilla, E.A.; Corbett, J.D. Hydrogen stabilization: Nine isotypic orthorhombic A_5Pn_3H phases (among A = Ca, Sr, Ba, Sm, Eu, Yb; Pn = Sb, Bi) formerly described as binary β-Yb_5Sb_3-type compounds. *J. Alloys Compd.* **1998**, *265*, 104–114. [CrossRef]

20. Leon-Escamilla, E.A.; Corbett, J.D. Hydrogen in Polar Intermetallics. Binary Pnictides of Divalent Metals with Mn_5Si_3-type Structures and Their Isotypic Ternary Hydride Solutions. *Chem. Mater.* **2006**, *18*, 4782–4792. [CrossRef]

21. Leon-Escamilla, E.A.; Stassi, P.D.C.; D, J. Corbett, Hydrogen in polar intermetallics: Syntheses and structures of the ternary $Ca_5Bi_3D_{0.93}$, $Yb_5Bi_3H_x$, and $Sm_5Bi_3H_{\sim 1}$ by powder neutron or single crystal X-ray diffraction. *Solid State Chem.* **2010**, *183*, 114–119. [CrossRef]

22. Gingl, F.; Vogt, T.; Akiba, E. Trigonal $SrAl_2H_2$: The first Zintl phase hydride. *J. Alloys Compd.* **2000**, *306*, 127–132. [CrossRef]

23. Björling, T.; Noréus, D.; Jansson, K.; Andersson, M.; Leonova, E.; Edén, M.; Hålenius, U.; Häussermann, U. SrAlSiH: A Polyanionic Semiconductor Hydride. *Angew. Chem. Int. Ed.* **2005**, *44*, 7269–7273. [CrossRef] [PubMed]

24. Werwein, A.; Auer, H.; Kuske, L.; Kohlmann, H. From Metallic *LnTt* (*Ln* = La, Nd; *Tt* = Si, Ge, Sn) to Electron-precise Zintl Phase Hydrides *LnTt*H. *Z. Anorg. Allg. Chem.* **2018**, *644*, 1532–1539. [CrossRef]

25. Brauer, G.; Haag, H. Über Darstellung und Kristallstruktur der Disilicide von einigen Metallen der Seltenen Erden. *Z. Anorg. Allg. Chem.* **1952**, *267*, 198–212. [CrossRef]

26. Bohmhammel, K.; Henneberg, E. Hydriding and dehydriding behavior of lanthanum silicides. *Solid State Ion.* **2001**, *141–142*, 599–602. [CrossRef]

27. Harris, I.R.; Mansey, R.C.; Raynor, G.V. Rare earth intermediate phases: III. The cubic laves phases formed with aluminium and cobalt. *J. Less-Common Met.* **1965**, *9*, 270–280. [CrossRef]

28. Franz, A.; Hoser, A. E9: The Fine Resolution Powder Diffractometer (FIREPOD) at BER II. *J. Large-Scale Res. Facil.* **2017**, *3*, A103. [CrossRef]

29. Rietveld, H.M. Line profiles of neutron powder-diffraction peaks for structure refinement. *Acta Cryst.* **1967**, *22*, 151–152. [CrossRef]

30. Rietveld, H.M. A profile refinement method for nuclear and magnetic structures. *J. Appl. Crystallogr.* **1969**, *2*, 65–71. [CrossRef]

31. Bruker AXS, TOPASc Version 5. Available online: www.bruker-axs.com (accessed on 28 March 2019).

32. Rodrıguez-Carvajal, J. Recent advances in magnetic structure determination by neutron powder diffraction. *Physica B* **1993**, *192*, 55–69. [CrossRef]

33. Rodrıguez-Carvajal, J. FullProf.2k, Version 5.30—Mar2012-ILL JRC. Institut Laue-Langevin: Grenoble, France, 2018.

34. *VESTA—Visualisation for Electronic and Structural Analysis*; Version 3.3.1; Koichi Momma and Fujio Izumi: Tokyo, Japan, 2018.

35. Momma, K.; Izumi, F. VESTA 3 for three-dimensional visualization of crystal, volumetric and morphology data. *J. Appl. Crystallogr.* **2011**, *44*, 1272–1276. [CrossRef]

36. Abinit v. 8.8.2, GNU General Public License. Available online: http://www.abinit.org (accessed on 28 March 2019).

37. Gonze, X.; Beuken, J.-M.; Caracas, R.; Detraux, F.; Fuchs, M.; Rignanese, G.-M.; Sindic, L.; Verstraete, M.; Zerah, G.; Jollet, F.; et al. First-principles computation of material properties: The ABINIT software project. *Comput. Mater. Sci.* **2002**, *25*, 478–492. [CrossRef]

38. Gonze, X. A brief introduction to the ABINIT software package. *Z. Kristallogr. Cryst. Mater.* **2005**, *220*, 558–562. [CrossRef]

39. Gonze, X.; Amadon, B.; Anglade, P.-M.; Beuken, J.-M.; Bottin, F.; Boulanger, P.; Bruneval, F.; Caliste, D.; Caracas, R.; Côté, M.; et al. ABINIT: First-principles approach to material and nanosystem properties. *Comput. Phys. Commun.* **2009**, *180*, 2582–2615. [CrossRef]

40. Gonze, X.; Jollet, F.; Araujo, F.A.; Adams, D.; Amadon, B.; Applencourt, T.; Audouze, C.; Beuken, J.-M.; Bieder, J.; Bokhanchuk, A.; et al. Recent developments in the ABINIT software package. *Comput. Phys. Commun.* **2016**, *205*, 106–131. [CrossRef]

41. Perdew, J.P.; Burke, K.; Ernzerhof, M. Generalized Gradient Approximation Made Simple. *Phys. Rev. Lett.* **1996**, *77*, 3865–3868. [CrossRef] [PubMed]

42. Blöchl, P.E. Projector augmented-wave method. *Phys. Rev. B* **1994**, *50*, 17953–17979. [CrossRef]

43. JTH PAW Atomic Datasets, Version 1.0. Available online: https://www.abinit.org/downloads/PAW2 (accessed on 28 March 2019).

44. Jollet, F.; Torrent, M.; Holzwarth, N. Generation of Projector Augmented-Wave atomic data: A 71 element validated table in the XML format. *Comput. Phys. Commun.* **2014**, *185*, 1246–1254. [CrossRef]

45. Monkhorst, H.J.; Pack, J.D. Special points for Brillouin-zone integrations. *Phys. Rev. B* **1976**, *13*, 5188–5192. [CrossRef]

46. Stadelmann, P.A. EMS—A software package for electron diffraction analysis and HREM image simulation in materials science. *Ultramicroscopy* **1987**, *21*, 131–146. [CrossRef]

47. JEMS Version 4.4631U. JEMS-SAAS: Saas-Fee, Switzerland, 2016.

48. Villars, P.; Calvert, L.D. *Pearson's Handbook of Crystallographic Data for Intermetallic Phases 1*; American Society for Metals: Metals Park, OH, USA, 1985; ISBN 0-87170-217-7.

49. Villars, P.; Calvert, L.D. *Pearson's Handbook of Crystallographic Data for Intermetallic Phases 2*; American Society for Metals: Metals Park, OH, USA, 1985; ISBN 0-87170-217-7.

50. Shashikalaa, K.; Sathyamoorthy, A.; Raj, P.; Dhar, S.K.; Malik, S.K. Structure and magnetic properties of $CeGa_2D_{0.6}$ system. *J. Alloys Compd.* **2007**, *436*, 19–22. [CrossRef]

51. Andresen, A.F.; Otnes, K.; Maeland, A.J. Neutron scattering investigations of $Be_2ZrH_{1.5}$ and $Be_2ZrD_{1.5}$. *J. Less-Common Met.* **1983**, *89*, 201–204. [CrossRef]

52. Bronger, W.; Chi-Chien, S.; Müller, P. Die Kristallstruktur von Bariumhydrid, ermittelt über Neutronenbeugungsexperimente an BaD_2. *Z. Anorg. Allg. Chem.* **1987**, *545*, 69–74. [CrossRef]

53. Brese, N.E.; O'Keeffe, M.; von Dreele, R.B. Synthesis and crystal structure of SrD_2 and SrND and bond valence parameters for hydrides. *J. Solid State Chem.* **1990**, *88*, 571–576. [CrossRef]

54. Denys, R.V.; Riabov, A.B.; Yartys, V.A.; Delaplane, R.G.; Sato, M. Hydrogen storage properties and structure of $La_{1-x}Mg_x(Ni_{1-y}Mn_y)_3$ intermetallics and their hydrides. *J. Alloys Compd.* **2007**, *446–447*, 166–172. [CrossRef]

55. Harms, W.; Wendorff, M.; Röhr, C. Mixed Alkaline Earth Trielides $A^{II}M1^{III}_xM2^{III}_{2-x}$ (A^{II} = Ca, Sr, Ba; M^{III} = Al, Ga, In). A Structural and Theoretical Study. *Z. Naturforsch.* **2006**, *62b*, 177–194. [CrossRef]

56. Björling, T.; Noréus, D.; Häussermannm, U. Polyanionic Hydrides from Polar Intermetallics AeE_2 (Ae = Ca, Sr, Ba; E = Al, Ga, In). *J. Am. Chem. Soc.* **2006**, *128*, 817–824. [CrossRef] [PubMed]

57. Evans, M.J.; Wu, Y.; Kranak, V.F.; Newman, N.; Garcia-Garcia, A.R.F.J.; Häussermann, U. Structural properties and superconductivity in the ternary intermetallic compounds MAB (M = Ca, Sr, Ba; A = Al, Ga, In; B = Si, Ge, Sn). *Phys. Rev. B* **2009**, *80*, 064514. [CrossRef]

58. Evans, M.J.; Holland, G.P.; Garcia-Garcia, F.J.; Häussermann, U. Polyanionic gallium hydrides from AlB_2-type precursors $AeGaE$ (Ae = Ca, Sr, Ba; E = Si, Ge, Sn). *J. Am. Chem. Soc.* **2008**, *130*, 12139–12147. [CrossRef] [PubMed]

59. Van Vleck, J.H. The Dipolar Broadening of Magnetic Resonance Lines in Crystals. *Phys. Rev.* **1948**, *74*, 1168–1183. [CrossRef]

60. Lee, M.H.; Björling, T.; Hauback, B.C.; Utsumi, T.; Moser, D.; Bull, D.; Noréus, D.; Sankey, O.F.; Häussermann, U. Crystal structure, electronic structure, and vibrational properties of MAlSiH (M = Ca, Sr, Ba): Hydrogenation-induced semiconductors from the AlB_2-type alloys MAlSi. *Phys. Rev. B* **2008**, *78*, 195209. [CrossRef]